Cadmium Sulphide Nanoparticles Decorated with Au Quantum Dots as Ultrasensitive

Photoelectrochemical Sensor for Selective Detection of Copper(II) Ions

Izwaharyanie Ibrahim[1], Hong Ngee Lim[1,2*], Osama K. Abou-Zied[3**], Nay Ming Huang[4], Pedro

Estrela[5], Alagarsamy Pandikumar[6]

[1] Department of Chemistry, Faculty of Science, Universiti Putra Malaysia, 43400 UPM Serdang,

Selangor, Malaysia

[2] Functional Device Laboratory, Institute of Advanced Technology, Universiti Putra Malaysia,

43400 UPM Serdang, Selangor, Malaysia

[3] Department of Chemistry, Faculty of Science, Sultan Qaboos University, P.O. Box 36, Postal

Code 123, Muscat, Sultanate of Oman

[4] Centre of Printable Electronics, Deputy Vice Chancellor Office (Research & Innovation),

University of Malaya, 50603 Kuala Lumpur, Malaysia

[5] Department of Electronic & Electrical Engineering, University of Bath, Bath BA2 7AY, United

Kingdom

[6] Research Institute & Department of Chemistry, Faculty of Engineering and Technology, SRM

University Kattankulathur, Chennai- 603 203, Tamil Nadu, India

*Corresponding Author (Hong Ngee Lim) - Phone: +603 8946 7494, E-mail:
janetlimhn@gmail.com

**Corresponding Author (Osama K. Abou-Zied) - Phone: +968 2414 1468, E-mail:
abouzied@squ.edu.om

Abstract

Anomalous ingestion of copper has significant adverse effects and shows acute toxicity in living organisms. Recently, photoelectrochemical (PEC) method has attracted much attention as a platform for a Cu^{2+} ion sensor because of its high sensitivity, selectivity, low-cost, and accurate selection compared to other conventional methods. In this work, stepwise hydrothermal and *in situ* chemical approaches for synthesizing cadmium sulphide nanoparticles (CdS NPs) for decorating gold quantum dots (Au QDs) are presented, along with a notable PEC performance. The amount of Au QDs loaded on the CdS NPs had a significant influence on the PEC performance. CdS NPs-Au QDs-2 with 1.0 mmol% of Au QDs demonstrated an exceptional photocurrent density of 350.6 μA cm^{-2}, which was 3.7, 2.2, and 2.0-fold higher than those of CdS NPs, CdS NPs-Au QDs-1 (0.75 mmol%), and CdS NPs-Au QDs-3 (1.25 mmol%), respectively. Femtosecond transient absorption dynamics of the ground state recovery showed a buildup time of 243 fs for Au and 268 fs for CdS, which were assigned to cooling of the photoexcited electrons. For CdS NPs-Au QDs, the transient spectrum was dominated by a signal from CdS with no contribution from Au. The fast buildup dynamic was absent in CdS-Au, indicating a rapid transfer of the photoexcited electrons from CdS to Au before cooling down. Unquestionably, the CdS NPs-Au QDs-2 photoelectrode response upon Cu^{2+} detection showed the lowest limit of detection of 6.73 nM in a linear range of 0.5–120 nM. The selectivity of CdS NPs-Au QDs-2 toward Cu^{2+} ions in lake and tap water was also studied, which suggested that CdS NPs-Au QDs-2 is promising as a photoactive material for PEC-based environmental monitoring and analysis.

1. Introduction

The rapid population growth and industrialization have led to severe environmental problems. The increasing number of environmental issues is beyond control when we cannot find practical solutions to address these problems [1]. However, current advances in nanotechnology may offer promising approaches to monitoring these environmental issues. Furthermore, the intriguing physicochemical properties of nanomaterials can be used to establish a good platform for numerous environmental applications such as sensors to detect various environmental pollutants. Although some high-tech analytical techniques and devices such as atomic absorption spectrometry (AAS), chromatography-mass spectrometry, and inductively coupled plasma mass spectrometry (ICP-MS) are capable of environmental monitoring and detecting miscellaneous trace pollutants, unfortunately, these devices require a high cost for equipment and maintenance, and also need a professional operator for machine handling [2]. Thus, there is an urgent necessity to develop devices with highly sensitive, selective, fast, affordable, and miniature sensors for the detection of environmental pollutants. A possible alternative to overcome the drawbacks of the aforementioned techniques is by using photoelectrochemical (PEC) measurement. This technique promotes a complete separation of the excitation source, a low background detection signal, and high sensitivity [3], thus providing a potential sensing platform that meets the current demand for a sensor system.

The PEC detection of copper ions (Cu^{2+}) has recently become an advanced technique for the environmental monitoring of superfluous copper consumption, which is found to cause serious toxicity for living organisms such as neurodegenerative disorder (Alzheimer's disease,

Transmissible Spongiform Encephalopathies (TSEs)) and severe liver diseases (Wilson's disease, Cirrhosis). This is not only a concern for human beings, but it also causes serious problems for animals and bacteria, because high concentration of Cu^{2+} can kill the biological retreatment systems in water by depressing the self-purification ability of natural waters [4]. Although the conventional methods (e.g., ICP-MS and AAS) for the detection of Cu^{2+} can also detect this trace element at low-quantity levels, a number of shortcomings, including expensive instruments, extremely time-consuming processes, and sophisticated operations, have made it urgent for researchers to find sustainable techniques in order to overcome these limitations. As previously mentioned, PEC is a promising technique for the detection of trace amounts of Cu^{2+}, with its environmental implications. Recently, several works have been reported on the PEC probing of Cu^{2+} ions with diverse combination of materials such as SnO_2/CdS heterostructural films [4], ZnO/CdS hierarchical nanospheres [5], Fe_2O_3-CdS heterostructures [6] and CdS-reduced graphene oxide (rGO) modified indium tin oxide (ITO) electrode [7], which illustrated an excellent selective interaction between the immobilized hybrid material on electrode and Cu^{2+} ions in the solution. Hence, the interaction between the hybrid material and Cu^{2+} ions exhibit the formation of Cu_xS-doped CdS, which resulted in an effective recombination of electron-hole, leading to decrease of photocurrent response. The Fe_2O_3-CdS photoanode [6] demonstrated a higher photocurrent density (~0.9 mA cm^{-2}) than ZnO/CdS hierarchical nanospheres [5] (~ 30 μA) in PBS of pH 7.4 at 0V vs Ag/AgCl under the simulated sunlight (100 mW^{-2}), and the intense photocurrent density resulted in an accurate detection of Cu^{2+} ions. Nevertheless, the Cu^{2+} sensor probe using Fe_2O_3-CdS photosensor is restricted to natural and basic aqueous medium because Fe_2O_3 is easily corroded in an acidic solution [8]. rGO is widely used because it is rich in structural defects and its chemical groups facilitate the charge transfer process and thus guarantee high

electrochemical activity. Consequently, the assembling of CdS on the surface of rGO enhances the electrochemical sensing performance and thus intensifies the photocurrent response through the synergic effects between CdS and rGO [7]. Even though much concern and effort have been devoted to this study, advanced nanomaterials with superior photocatalytic performances are necessary in order to develop more robust and sensitive PEC sensors. These nanosized materials enhance the total surface area and subsequently increase the number of reaction sites available for PEC sensing to take place [9].

Recently, the field of nanotechnology has attracted extensive interest in modern chemistry and has been rapidly increasing. Following the current advances in nanotechnology, extremely sensitive nanosensors can be designed using nanomaterials. The dimensions of the nanomaterials are on the nanometer scale (≤100 nm range) and apparently show their novel properties, compared to bulk materials [10], thus offering unique superior properties for optical, electronic, magnetic, and catalytic effects. The huge modification of the physiochemical properties upon the transition of microparticles to NPs has been the center of attention among researchers when synthesizing NPs [11]. Furthermore, hybrids of NPs offer unique physicochemical properties that are attracting more and more attention [12]. NP hybrids with semiconductors, decorated by metal quantum dots (QDs), have provided another method to modify the properties of NPs as a result of their size-dependent properties and thus offer advantages in numerous aspects of nanotechnology [13].

A large number of the existing semiconductor photocatalysts can only be excited under ultraviolet irradiation because of the wide band gap properties of the photocatalyst [14]. In order to address this limitation, much effort to develop a semiconductor that only shows a response to visible light has been expended because of the advantages of availability and abundant solar

spectrum in the universe. Among the many available semiconductors, much attention has been paid to CdS because of its superior advantages such as an appropriate band gap of 2.4 eV, which matches well with the solar spectrum [15]. Furthermore, CdS NPs have their own importance because of their vast range of applications in electronics and photonics such as photosensors [16], DNA sensors [17], gas sensors [18], and solar cells [19]. Nevertheless, hybrids of CdS NPs with another material allow the properties to be tuned to make them useful in other research areas. Therefore, much effort has gone into assembling noble metals (e.g., Au, Ag, Pt, and Pd) on the surfaces of spherical CdS NPs to further enhance the sensitivity of the sensing materials. The development of Au which induced plasmonic effect on photo-active materials like CdS semiconductors has prompted an intensive interest in PEC applications [20-21], photocatalysis [22], and solar cells [23]. According to Xing *et al.*, a unique and distinctive interaction phenomenon involving the transportation of electrons and energy will take place when CdS and Au are in close contiguity under some conditions [24]. The decoration of Au QDs on the surface of CdS NPs resulted in the amplification of photocurrent signal because of an enhance absorption of photon generated photoelectron on the CdS [25]. Therefore, it provides a high-throughput detection system and subsequently prompts in the readout of produced photocurrent signal. Even though a lot of efforts have been reported in the utilization of hybrid structure CdS-Au in detecting biomarkers [26-27], only a few works have been reported for sensing of heavy metal ions based on label-free method [28-29]. To the best of our knowledge, there is a gap on employing CdS NPs-Au QDs as a PEC sensing electrode material for Cu^{2+} ions detection.

In this study, a favorable selective PEC sensor was fabricated based on CdS NPs hybrid Au QDs and utilized as a system for tracing Cu^{2+} amounts. The photoelectrode model of CdS NPs decorated on Au QDs was fabricated by a stepwise accumulation of CdS NPs and Au QDs,

which acted as a PEC sensor with excellent anti-interference ability. The new CdS NPs-Au QDs deposited on indium tin oxide (ITO) were further manifested as the rationalization of a hybrid structure containing nanomaterials that could be used to modify the Cu^{2+} photosensors with an extremely fast response, high sensitivity, and selectivity. Moreover, on the basis of the CdS NPs-Au QDs as a photosensor probe, this work reported on an advanced plasmonic PEC study that is capable of amplifying a label-free PEC sensor. The applicability of the PEC approach in Cu^{2+} sensing was subsequently attempted on real samples from lake water and tap water. The current work had the benefit of practically utilizing CdS NPs-Au QDs nanomaterials as a probe in the area of environmental monitoring of trace metal elements.

2. Experimental Methods

2.1. Materials

Copper (II) sulfate pentahydrate ($CuSO_4.5H_2O$) and cadmium acetate dihydrate ($Cd(CH_3COO)_2 \cdot 2H_2O$) were purchased from Hamburg Chemicals, Germany. Thiourea (CH_4N_2S) was purchased from Fisher Scientific, USA. Chloroauric acid ($HAuCl_4.3H_2O$) and trisodium citrate ($Na_3C_6H_5O_7$) were purchased from Aldrich, USA. Acetone ($(CH_3)_2CO$, 99.5%) was purchased from Friendemann Schmidt, USA. Ethanol ($CH_3CH_2OH_2$, 95%) was purchased from Systerm, Malaysia. Potassium chloride (KCl) and triethanolamine (TEA, 99%) were obtained from Merck, USA. Indium tin oxide (ITO) conducting glass slides (7 Ωsq^{-1}) were commercially supplied by Xin Yan Technology Limited, China. Each stock solution of Zn^{2+}, Mn^{2+}, Na^+, Ba^{2+}, Mg^{2+}, K^+, Ni^{2+}, Co^{2+}, Fe^{2+}, and Cr^{2+} was composed of dissolved appropriate amounts of the compounds ($ZnSO_4.7H_2O$, $MnSO_4.H_2O$, $NaCH_3OO$, $BaCl_2.2H_2O$, $MgCl_2.6H_2O$, KCH_3CO_2, $NiSO_4$, $CoSO_4$, $FeSO_4$, and $Cr_2(SO_4)_3.15H_2O$) in Milli-Q deionized water with a

resistivity of 18.2 MΩ cm. Each sample solution was 10 mL. Deionized water was used in all the experiments. Unless otherwise specified, all the materials and reagents were used as received without conducting any purification process.

2.2. Preparation of CdS NPs

The hydrothermal process for the synthesis of CdS NPs was carried out by mixing 0.30 M $Cd(CH_3COO)_2 \cdot 2H_2O$ and 0.18 M CH_4N_2S aqueous solutions. Then, 50 wt% triethanolamine was dissolved completely into the mixture. The mixture was stirred for 2 h to confirm the cooperative interaction and self-assembly process. The final mixture was placed in a Teflon autoclave, sealed tightly, and subjected to a hydrothermal reaction at 180 °C for 24 h. The final attained CdS NPs solution was centrifuged and thoroughly washed with ethanol and deionized water in order to discard the residual organic matter and ions. Finally, the precipitates were dried at room temperature for 24 h to yield yellow powders.

2.3. Preparation of Au QDs

Au QDs were synthesized by the citrate reduction of $HAuCl_4$ [30]. Briefly, 50 mL of 1.0 mmol% $HAuCl_4$ salt was placed into a round bottom flask of a reflux system. The solution was heated until boiling. Under continuous stirring, trisodium citrate solution (1.0% w/v in 2.0 mL) was slowly added. The solution color changed from pale yellow to black and finally turned to a red wine color over several minutes. The reflux reaction then occurred for 1 h. After the solution was cooled down, it underwent a filtration process through a nylon membrane with a pore size of 0.22 μm. For comparison, different concentrations of Au QDs (0.75, 1.0, and 1.25 mmol%) were prepared.

2.4. Preparation of CdS NPs-Au QDs

CdS NPs-Au QDs were prepared using the reflux approach. Here, 50 ml of 1.0% w/v of freshly prepared CdS powder was mixed with the Au QDs solution with various loading concentrations of 0.75, 1.0, and 1.25 mmol% and the samples were labeled CdS NPs-Au QDs-1, CdS NPs-Au QDs-2, and CdS NPs-Au QDs-3, respectively. The mixture was left for 24 h to grow the Au QDs over the CdS NPs. Afterward, the solution was placed in a three-necked flask and directly heated at 100 °C in a reflux system in a nitrogen gas atmosphere for 1 h. This step was conducted in order to grow the Au QDs on the CdS NPs structure. A final dark yellow colloidal solution was obtained. After cooling down, the resultant mixture was centrifuged and washed with ethanol and deionized water three times. Lastly, the precipitates were dried at room temperature for 24 h to yield dark yellowish powders of CdS NPs-Au QDs.

2.5. Characterization Techniques

The morphologies of the nanomaterials were characterized using a field emission scanning electron microscope (FEI Quanta SEM Model 400 F) equipped with an energy dispersive X-ray (EDX) accessory and transmission electron microscopy (TEM) (Hitachi, HT-7700). The crystalline phase of the CdS NPs-Au QDs was analyzed using a Philips X'pert system X-ray powder diffractometer with Cu Kα radiation (λ = 1.5418 Å), and the optical absorption properties in the spectral region of 200–800 nm were assessed using a UV-Vis spectrophotometer (Thermo Scientific Evolution 300). A photoluminescence analysis was conducted using a Renishaw inVia Raman microscope with laser excitation at λ = 514 nm.

Ultrafast transient absorption measurements were conducted using a femtosecond laser source (Libra, Co-herent) that contained a diode-pumped, mode-locked Ti:Sapphire oscillator (Vitesse. Fundamental 800 nm), amplified by a diode-pumped intracavity doubled Nd:YLF laser

(Evolution). The Libra generated compressed laser pulses (90 fs pulse width) with an output of 4.26 W at a repetition rate of 5 kHz. The output beam was split into two parts. A small portion was used as the gate pulse (vide infra), while the major portion of the output pulse was used to pump a Coherent OPerA Solo (Light Conversion Ltd.) optical parametric amplifier to generate spectrally tunable light spanning the range of 240−2600 nm, which was used as the pump beam.

A Helios transient absorption spectrometer (Ultrafast Systems LLC) was used for the optical detection. The source for the pump and probe pulses was derived from the output of the Libra. A small portion of the output pulse was focused on a sapphire crystal to generate a white light continuum in the range of 430–800 nm, which was used as the gate pulse. The probe light was measured using an optical fiber that was coupled to a multichannel spectrometer with a CMOS sensor in the range of 350–850 nm. The sensor had a 1.5 nm intrinsic resolution. The repetition rate of the laser was reduced to 1 kHz in order to match the working parameters of the Helios. A chopper was used to block every other pump pulse (~3 mm diameter), thus generating 500 Hz sync signals.

The rotational contribution to the overall excited state decay kinetics was removed by depolarizing the pump beam using a depolarizer (DPU-25, Thorlabs). In this way, the excited molecules' absorption was isotropic, and therefore any dipole-dipole interactions between the excited molecules and the probe light were cancelled out. The pump pulse was attenuated to ~150–200 nJ in order to avoid multiphoton excitation and ensure a one-photon absorption process[31-33].

The pump and probe pulses were focused on the sample, which was placed in a cylindrical cell with a path length of 2 mm. The relative temporal delay between the pump and

probe pulses was varied in 20 fs steps, using a computer-controlled linear stage (retro reflector in a double pass setup). Kinetic traces at appropriate wavelengths were assembled from the time-resolved spectral data. Surface Xplorer software (supplied by Ultrafast Systems) was used for the data analysis. The wavelength dependence of the coherent artifact signal from the pure solvent was used for the time-zero correction of the time-resolved absorption data and to determine the instrument response. The latter was estimated to be ~150 fs (dashed curve in Fig. 4A). The steady-state absorption spectra of the samples were compared before and after the experiments, and no changes were observed in the absorbance and spectral shape, indicating no photodegradation effect due to the laser pulses.

2.6. Preparation of Photoelectrochemical Sensor Electrodes

The CdS NPs-Au QDs/ITO-modified sensor electrode was prepared using a simple doctor blade method. First, an ITO glass substrate (2 cm × 2 cm) was cleaned ultrasonically using acetone, ethanol, and deionized water. After that, 0.5 ml of the 50% w/v CdS NPs-Au QDs powder was mixed with a nafion solution (0.1% w/v), and the mixture was stirred for several minutes to disperse the CdS NPs-Au QDs powder. Then, the CdS NPs-Au QDs paste was cast onto the ITO glass by a doctor blade with tape as the spacer. The resultant CdS NPs-Au QDs thin film was dried at 100 °C and calcined at 150 °C for 1 h in an inert atmosphere. For comparison, CdS NPs/ITO and Au QD/ITO-modified electrodes were also fabricated by following the same procedure.

2.7. Photoelectrochemical Experiments

The photoelectrochemical detections were performed with a three-electrode system that included the active material as the working electrode, a platinum wire as the auxiliary electrode,

and a Ag/AgCl electrode as the reference electrode. Here, 0.1 M KCl containing 0.5 M TEA as the electron donor was used as an electrolyte. A 150-W halogen lamp (Halloid) was used as the light source in this experiment. Before the PEC test, the samples were carefully washed with 0.1 M KCl and immersed in the electrolyte for 10 min to fully remove the absorption molecules. Immediately after the background photocurrent was stabilized, the photocurrent response was recorded while the excitation light was turned on and off. The photocurrent signal was measured and analyzed on a computer-controlled Versa-STAT-3 electrochemical analyzer from Princeton Applied Research.

3. Results and Discussion

3.1. Structure Characterization of CdS NPs-Au QDs

The morphology characteristics of the nanostructures of the obtained materials were verified using FESEM and TEM. Fig. 1A shows FESEM images of the CdS NPs-Au QDs prepared by the stepwise assembly method. It is observed that the CdS and Au are successfully synthesized in the hydrothermal and *in situ* combination process because the CdS appears to have a corrugated surface due to the presence of Au (Fig. 1A). The successful preparation of the synthesized materials was also varied by the EDX spectrum (see supplementary information, Fig. S1A), which reveals the existence of the Cd, S, and Au elements, thus confirming the successful preparation of the materials. The size distribution graph shown in the inset of Fig. 1A illustrates the uniformly distributed CdS NPs-Au QDs with average particle diameters of 25–30 nm. Referring to Fig. 1B, the Au QDs were decorated on the CdS NPs, which is in contrast with the flawless structures of the neat CdS (see supplementary information, Fig. S1B). The pre-synthesized Au QDs prepared via citrate reduction were demonstrated to readily attach on the

surface of the as-synthesized CdS NPs. Therefore, this convincingly reveals that the Au and CdS were successfully prepared in 1 h by the reflux system. The selected area in the electron diffraction (SAED) pattern in the inset of Fig. 1B indicates that the CdS-Au QDs had a polycrystalline structure. The SAED pattern forms an area that presents the lattice planes of (111) and (112), which represent the CdS NPs, and (220) represents the Au QDs [34], both of which are in agreement with the polycrystalline structure of CdS-Au. Moreover, the TEM image (Fig. 1C) highlights the lattice fringes present on the NPs, with a distance of 0.327 nm, and on the QDs, with a distance of 0.373 nm, which agree well with the d-spacing of the hexagonal wurtzite CdS (101) and plane cubic Au (200) crystallographic planes, respectively.

In addition, the crystalline properties and phase structures of the products were further analyzed and investigated using X-ray diffraction (XRD). In Fig. 1D, the sharp and strong diffraction of the XRD peaks exhibit high-quality crystallization [35]. Comparing these three diffraction peaks, the crystallinity of the CdS NPs and Au QDs show similar or sharper peaks than the CdS-Au nanostructures. The diffraction pattern of the CdS can be attributed to hexagonal wurtzite CdS with JCPDS No. 41-1049 and exhibits five main diffraction peaks at 23.6°, 26.8°, 30.4°, 48.2°, and 52.1°, which can be assigned to the (100), (002), (101), (110), and (112) planes, respectively. Compared with Au, the peaks at 36.5°, 43.9°, 64.5°, and 75.4° (green color) depicted in the diffraction pattern of the nanocomposite CdS-Au can be ascribed to cubic Au (JCPDS Card No. 04-0784), with the diffraction peak indexes from (111), (200), (220), and (311), respectively, indicating that the Au was successfully synthesized on the CdS NPs, which was rational with the SAED pattern obtained.
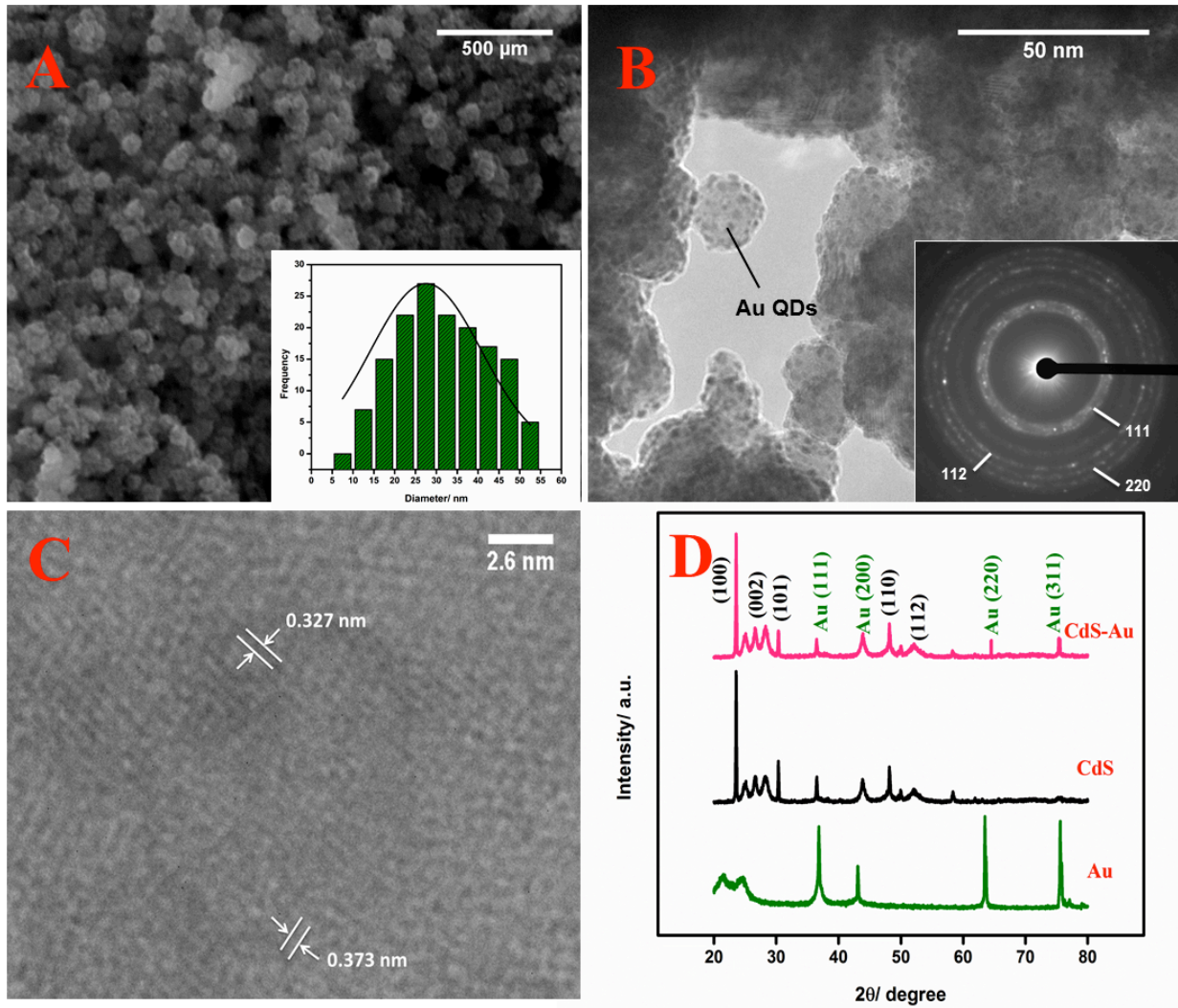
Fig. 1- (A) FESEM image with inset size distribution graph of CdS NPs-Au QDs; (B) TEM image of CdS NPs decorated on Au QDs with corresponding SAED pattern (inset); (C) lattice fringe showing CdS and Au crystals; and (D) XRD patterns of Au QDs, CdS NPs, and CdS NPs-Au QDs.

One of the focal characteristics of a semiconductor-metal is the optical-absorption signature. The surface plasmon resonance (SPR) band of the Au QDs, and CdS NPs-Au QDs are displayed in Fig. 2A. The Au QDs show the SPR band at 520 nm in the visible region. Moreover, the Au QDs show strong and narrow SPR band while the CdS NPs show a broad and weak band

in the visible region [36]. Compared to the pure Au QDs, in which the peak centers at 520 nm, the SPR absorption band of the hybrid CdS-Au is centered at 503 nm, and is broader and blue-shifted, which is a general phenomenon of such a hybrid material due to the high dielectric coefficient and exciton plasmon coupling on the CdS NPs by Au QDs [37]. On the other hand, when compared with the pure CdS NPs, in which the peak centers at 534 nm, the CdS-Au displays a narrower band. The broad band displayed for the CdS NP peak is due to a common circumstance of CdS surface state emission [38]. Meanwhile, the narrow band of CdS-Au is due to the SPR feature of Au QDs. Subsequently, we have calculated the size of the Au QDs from the SPR band observed from the absorption spectra by using the standard and well-known "Haiss equation" [39-42]. This Haiss equation (Eqn. 1) is more often used to calculate the particle size of the Au QDs/NPs from the SPR band of the absorption spectrum.

$$d = \frac{\ln{(\lambda_{spr} - \lambda_0)/L_1}}{L_2} \qquad \text{(Eqn. 1)}$$

where d is the diameter of the particle (nm), λ_{spr} (520 and 503 nm for Au QDs and CdS-Au, respectively) is the wavelength of the surface plasmon resonance band, $\lambda_0 = 512$ nm, $L_1 = 6.53$ and $L_2 = 0.0216$. Using this equation, the size of the Au QDs for pristine Au QDs and CdS-Au QDs were calculated as 9.40 and 14.85 nm, respectively from the absorption spectra.

In this study, we compared the photoluminescence (PL) spectra between pure CdS NPs and a nanocomposite of CdS-Au QDs, as displayed in Fig. 2B. The PL spectrum of the pure CdS NPs shows an emission peak at 527 nm and a shoulder at 487 nm. Subsequently, the remarkable quenching of the CdS-Au QDs PL emission is detected at a peak of ~518 nm compared with the enhanced CdS emission peak. The two-fold decrease in intensity for the CdS-Au QDs occurred because of the effective segregation of photogenerated electrons and holes. At a lower Fermi

energy level, the photogenerated electrons in the CdS NPs could easily be captured by the Au QDs and thus resulted in a decrease in the radiative recombination [37]. Moreover, the quenching result for the CdS-Au PL emission could also be the result of the SPR absorption effect [43] since the absorption peak of the Au NPs in Fig. 2A (519 nm) overlaps with the emission peak of CdS (527 nm). Consequently, the quenching of the PL emission when CdS was hybridized with Au QDs illustrated an improvement in electronic passivation and hence suggested the effective role of the Au QDs in hindering the surface recombination state [44]. More insights into the electron-hole recombination mechanism will be discussed below.
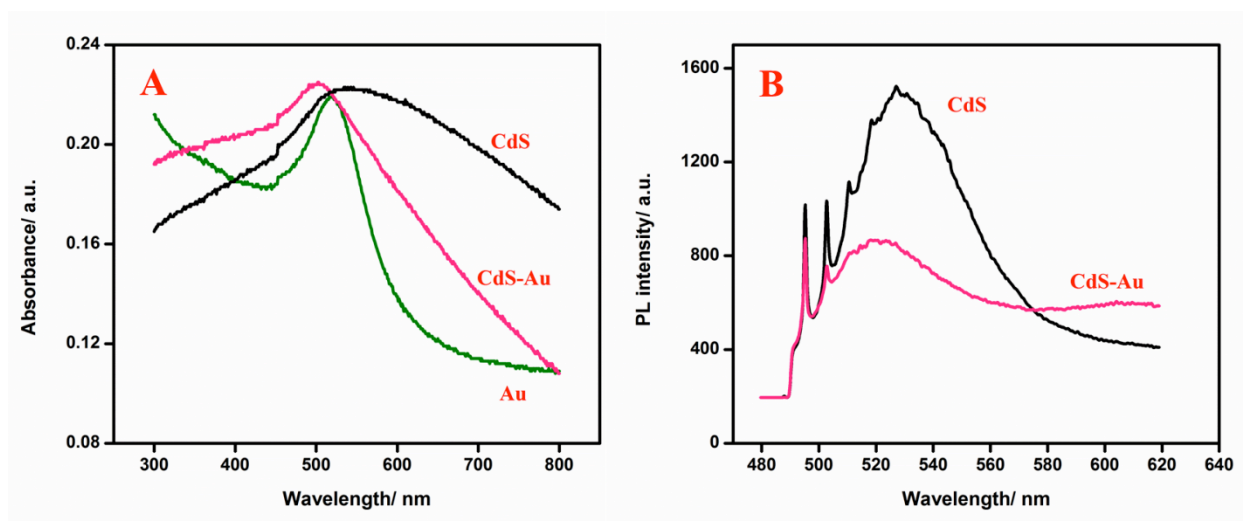
Fig. 2- (A) Ultraviolet visible absorption spectra and (B) PL spectra of CdS NPs, Au QDs, and CdS NPs-Au QDs.

3.2. Femtosecond-Nanosecond Transient Absorption Dynamics

The electronic transition and relaxation dynamics of the systems of Au QDs, CdS NPs, and CdS NPs-Au QDs were examined in the femtosecond to nanosecond time range by recording the absorbance change in real time. Fig. 3 shows the spectra for the three systems during the

16

initial period of 800 fs after excitation at 400 nm. The transient spectra for the Au QDs show positive absorbance wings around the bleach peak centered at ~525 nm. The two wings exhibit an instantaneous build up within the system response duration (~150 fs), followed by a decay at a constant time of about 2.8 ps. The two photoinduced absorbance bands are the results of the change in the dielectric constant and the increase in the electron temperature of the Au QDs, which result in the broadening of the SPR band [32-33]. The bleach band at 525 nm represents the temporal change in the SPR peak (see the steady state absorbance in Fig. 2B). For CdS NPs, the transient spectra at different delay times in Fig. 3 show a bleach band at 490 nm. The bleach bands for the Au QDs and CdS NPs reach a maximum buildup after 500 fs. For the CdS-Au system, the bleach band at 490 nm shows a dramatic change in behavior when compared to that of the CdS NPs. The initial buildup time of this band is absent in CdS-Au, and an overall lower intensity can be clearly noticed. The transient spectrum of CdS-Au is dominated by a signal from CdS, whereas the Au bleach band shows almost no contribution to the observed signal.
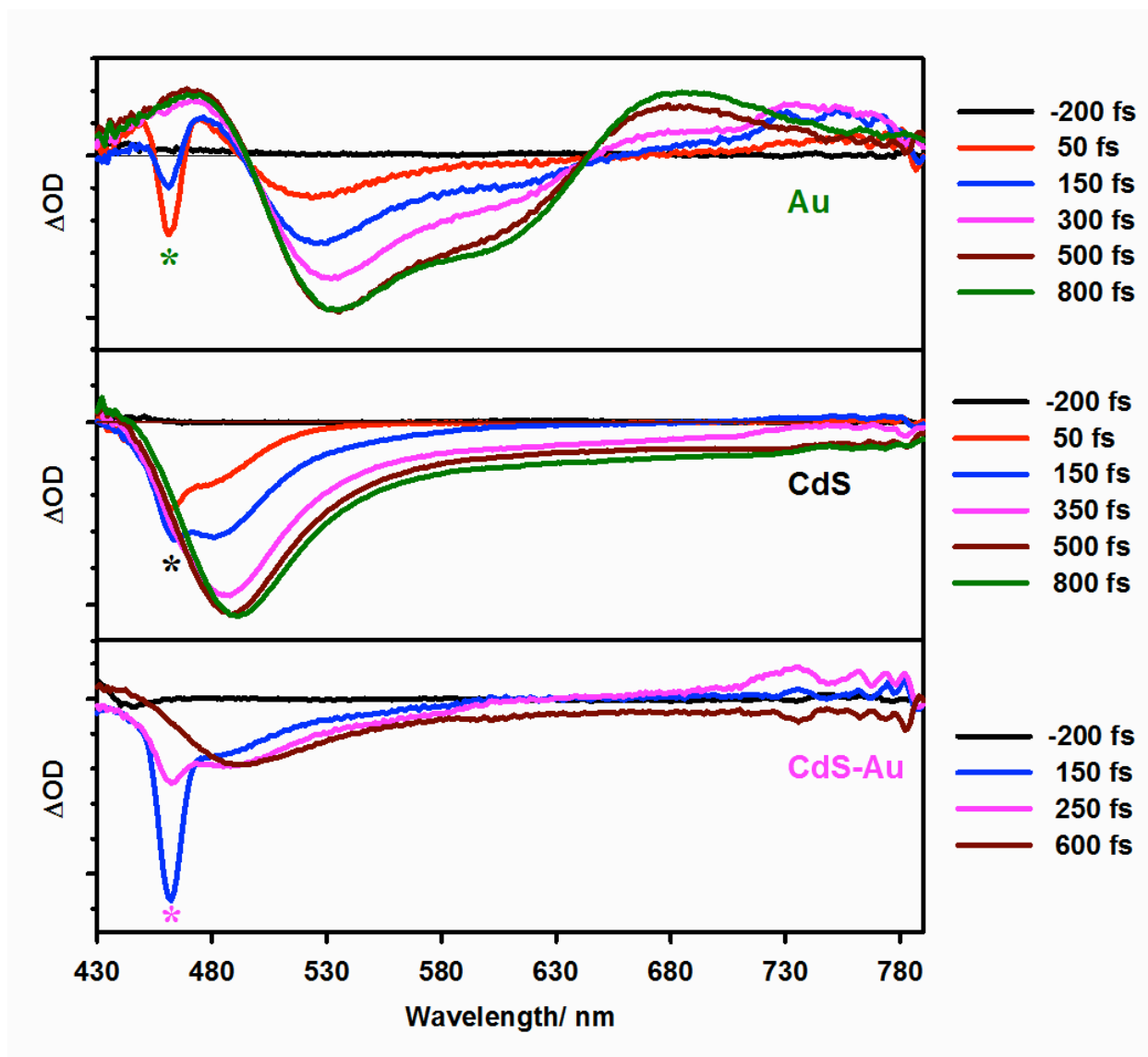
Fig. 3- Femtosecond transient absorption spectra of Au QDs, CdS NPs, and CdS NPs-Au QDs. The dynamics were recorded during the first 800 fs immediately after photoexcitation at 400 nm and * represents the Raman scattering due to the solvent.

More insight into the detailed dynamics of the bleach bands in the three systems are shown in the temporal profiles in Fig. 4 for up to 5 ns. For the Au QDs and CdS NPs, the transients in Fig. 4A show an increase in the bleach intensity during the first 500 fs period (note the sign of the intensity axis). The fits in Fig. 4A show the buildup in intensity as time constants

of ~243 fs for Au and ~268 fs for CdS. On the other hand, the transients for the CdS NPs-Au QDs indicate a prompt rise within the instrument response, with no apparent buildup time. The rise times for the Au QDs and CdS NPs are a consequence of the cooling dynamics of the photoexcited electrons (electron-electron interactions). The absence of this dynamic process in CdS-Au indicates that the photoexcited electrons in CdS-Au are rapidly transferred from the CdS to Au before cooling down.

The slower dynamics in the three systems reflect the bleach recovery, as depicted in Fig. 4B and Fig. 4C. For the Au QDs, this recovery is represented in the electron-photon interaction (2.38 ps) and finally the phonon-phonon interaction, which takes place in 85 ps [32-33]. In the CdS NPs, the bleach recovery shows multi-exponential dynamics that are represented by four decay time constants, as listed in Table 1. These decay dynamics were induced by the electron-hole recombination at different trapped depths [45]. As listed in Table 1, the four relaxation dynamics for the CdS NPs become much faster in the CdS NPs-Au QDs (with the exception of the first component, the three slowest time constants are ~50% faster). The latter results suggested the efficient transportation of the excited electrons from the semiconductor domain (CdS NPs) to the noble metal domain (Au QDs).
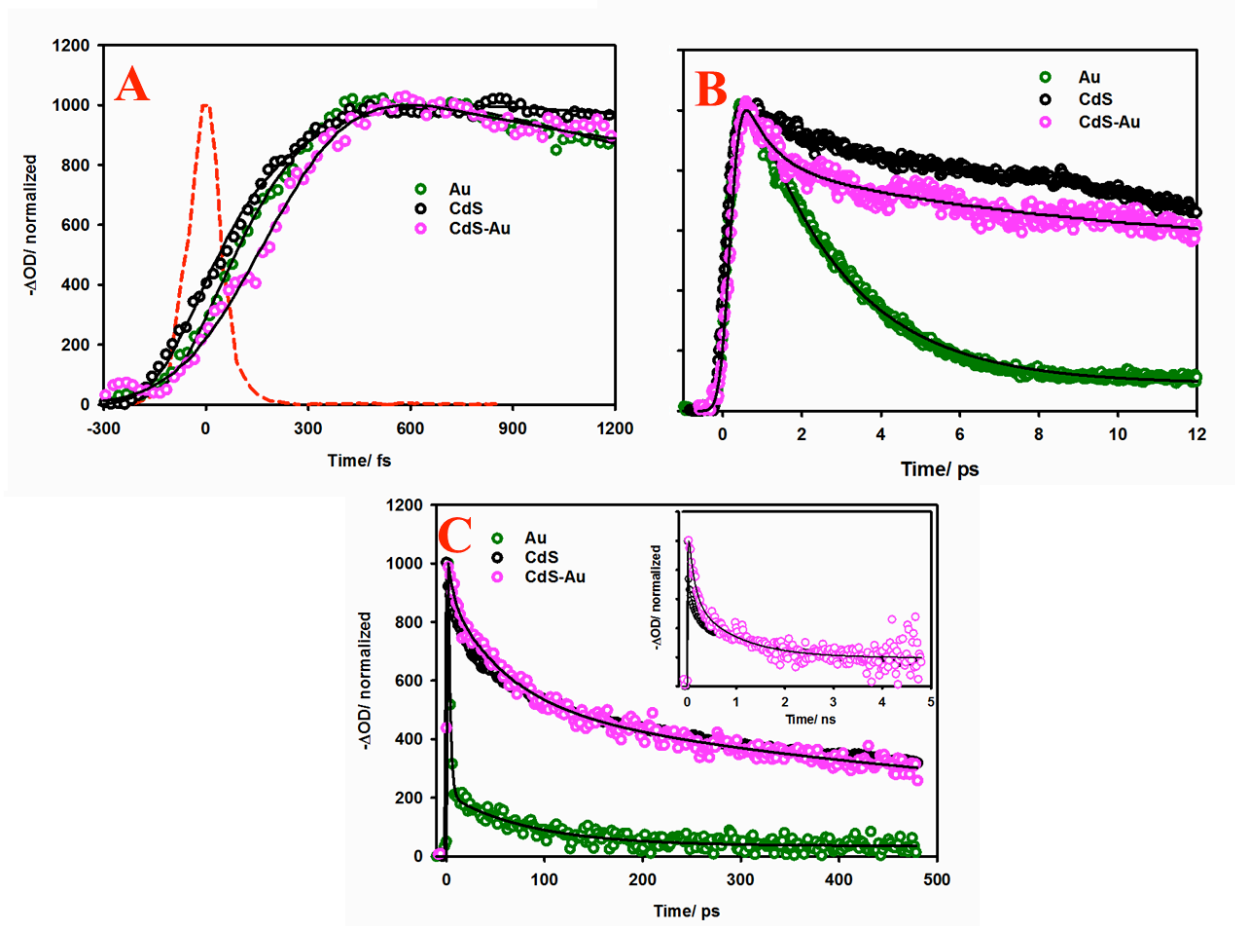
Fig. 4- Dynamics of Au QDs, CdS NPs, and CdS NPs-Au QDs derived from (A) femtosecond, (B) picoseconds, and (C) sub-nanosecond-nanosecond transient absorption spectra. The dashed line represents the system response measured from the Raman scattering of the solvent.

Table 1- Summary of transient absorption dynamics of Au QDs, CdS NPs, and CdS NPs-Au QDs (λ_{ex} = 400 nm).

Sample	$\tau_{(rise)}$ (fs)	τ_1 (ps)	τ_2 (ps)	τ_3 (ps)	τ_4 (ns)
Au λ_{det} = 530 nm	243 ± 17	2.38 ± 0.05	85.0 ± 2.0		
CdS λ_{det} = 490 nm	268 ± 20	0.73 ± 0.07	21.3 ± 1.0	110 ± 4	1.86 ± 0.03
CdS-Au λ_{det} = 490 nm		0.71 ± 0.07	9.6 ± 0.5	59 ± 2	0.95 ± 0.02

3.3. Excellent PEC Performance of CdS NPs-Au QDs

Fig. 5A demonstrates the current densities-potential responses of the as-prepared samples to evaluate their PEC activity and performance. Linear sweep voltammograms (LSV) were obtained under irradiation with 30 s on-off light cycles. As depicted in Fig. 5A, compared with CdS, the CdS-Au QDs exhibited a 3.8-fold larger photocurrent in the entire potential window and had a fast response with good photo-switching performance, as well as good photostability, thus indicating that the CdS-Au QDs possess better PEC performance. However, there was no photocurrent response detected for the single Au QDs under the visible light. Therefore, two conclusions can be drawn from the LSV analysis. First, the *in situ* assembly of Au QDs is an effective means for promoting the PEC performance of CdS NPs-Au QDs, and second, the synergic effect of the CdS NPs and Au QDs contributed to the significant photocurrent response.

Fig. 5B displays the response of the open-circuit photovoltage (V_{oc}) under the on-off light stimuli. V_{oc} represents the difference in the Fermi levels between the working electrode, where

the photoactive material was deposited, and the counter electrodes [46]. Under light irradiation, excited photoelectrons accumulate within the nanostructure (CdS or CdS-Au QDs) films, promoting a change in the apparent Fermi level to a less positive voltage. The inverse result demonstrated that the electrons (not holes) are transferred from the photoactive material to the ITO substrate through the electrolyte [47]. Once the illumination is blocked, the assembly of photoelectrons are slowly released because the electron acceptor species has been scavenged in the electrolyte, which leads to recombination with the photoholes [48]. Furthermore, the slow decay of the excited electrons indicates a larger and longer lifetime, which can aid the electron transfer without any losses at grain boundaries [46]. As expected, the CdS-Au QDs showed an elevated negative photovoltage response under irradiation and discharged slowly in the absence of light compared to CdS. This result suggested a more effective charge separation and decrease in the charge recombination for the CdS-Au QDs. Similar to the photocurrent density results, no photovoltaic response was observed for the Au QDs under on-off irradiation.

The Bode phase plots in Fig. 5C further support the above results. According to Equation (1), the electron lifetime (τ_e) can be evaluated using the maximum frequency peaks (f_{max}) in the Bode phase plots [49]:

$$\tau_e = 1/(2\pi\, f_{max}) \qquad (1)$$

As clearly shown in Fig. 5C, f_{max} shifted to a lower frequency region for single Au QDs, which achieved a μs-scale of τ_e = 400 μs, or about 6.3-fold slower than that of the hybrid CdS-Au QDs with a τ_e of 63.36 μs. Even though the lifetime is larger, Au QDs are not sensitive to light illumination, making them an inappropriate electrode for PEC detection because of poor photocurrent and photovoltaic signals. A comparison of the τ_e values of the CdS NPs and CdS-

Au QDs (Fig. 5D) shows that the f_{max} value of CdS decreases from 3162.28 to 2511.89 Hz after the introduction of Au QDs (CdS-Au QDs), illustrating that the electron lifetime increases from 50.33 μs to 63.36 μs. Therefore, the enhancement in the electron lifetime results in slower recombination and provides more chances for the occurrence of electron-hole separation. It was suggested that this result was responsible for the remarkable increase in the photocurrent density and the onset potential [48-49].
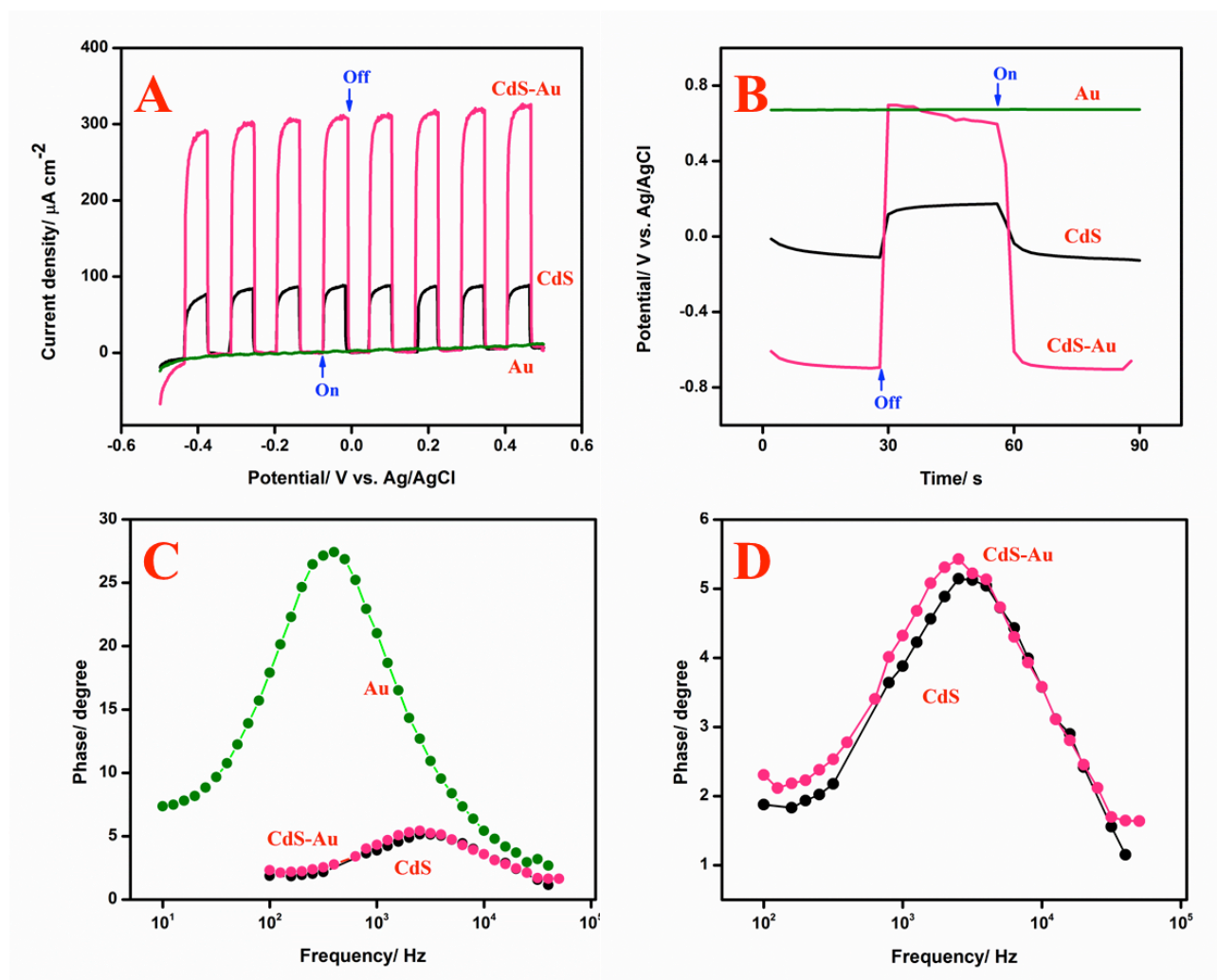
Fig. 5- (A) Photocurrent densities-potential graph and (B) open-circuit photovoltage responses under light on-off stimuli. (C) Bode-phase plots of the as-prepared electrode and (D) magnification of bode-phase plot of CdS NPs and CdS-Au QDs in 0.1 M KCl and 0.5 M TEA.

3.4. PEC Sensor Characterization

Electrochemical impedance spectroscopy (EIS) Nyquist plots were drawn for the modified photoelectrodes of pure CdS NPs and CdS NPs-Au QDs with different Au loadings, as illustrated in Fig 6A. EIS is a better tool for evaluating the chemical interfacial properties of photoelectrodes. The Nyquist plots of the EIS were recorded from 0.01 to 10^5 Hz at 0 V in 0.1 M KCl containing 5.0 mM $K_4[Fe(CN)_6]/K_3[Fe(CN)_6]$. In comparison with ITO (curve a), CdS (curve b) demonstrated a higher charge-transfer resistance (R_{ct}) of 19.0 Ω. This was because of the high electrical resistance of CdS, implying that this active material was successfully deposited onto the ITO substrate (R_{ct} =13.8 Ω). Obviously, the R_{ct} value was significantly reduced to 7.8 Ω after the successful formation of CdS NPs-Au QDs-1 (curve c), with an Au loading of 0.75 mmol% deposited on the surface of the electrode. This result was further justified because the positively charged Au QDs promoted the transfer of the negatively charged $Fe(CN)_6^{3-/4-}$ contained in the electrolyte [48]. Furthermore, the EIS responses of the fabricated PEC sensor toward different concentrations of Au QDs (curves d & e)) were further investigated. When the concentration of Au QDs is increased to 1.0 mmol% (curve d), the R_{ct} value shows the lowest semicircle of 5.8 Ω, indicating the optimum loading of Au that provides the fastest electron mobility. Nevertheless, the R_{ct} value appears to gradually increase (R_{ct} =13.6 Ω) when Au reaches 1.25 mmol% (curve e). This is because of the higher concentration of Au QDs that aggregate on the CdS NPs-Au QDs-3 surface, which hinder and limit the feasibility of the electron transfer process [50-51]. Hence, it is indicated that the CdS NPs-Au QDs-2 could not only

offer a compatible surface for loading and capturing Cu^{2+} ions but could also provide a sensitive electric interface for further sensing.

In order to determine the feasibility of this PEC sensor, the photocurrent responses of the as-prepared electrodes were investigated, and the results are displayed in Fig. 6B. Referring to curve b, the CdS NPs demonstrate a sensitive PEC response because of their small particle size, which provides a large specific surface area and more open structure, promoting effective interfacial charge capture and rapid electrolyte diffusion [48]. In addition, the fast response of the photocurrent densities illustrates an efficient charge separation and excellent electrical communication between the CdS NPs and the ITO substrate. In contrast, no PEC response is observed under the on-off light illumination for the bare Au QDs (curve f). Subsequently, the PEC response of the CdS NPs-Au QDs-1 modified electrode displayed in curve c shows a slight increase in the photocurrent intensity compared to the intensity value obtained for the CdS NPs photoelectrode. The enhancement in the photocurrent when Au is introduced on the spherical CdS NPs can be explained by an increase in scattering due to the presence of the metal. The increase in scattering allows the CdS to absorb more light and thus inject more electrons into the conduction band of CdS [52-53]. Expectedly, the CdS NPs-Au QDs-2 (curve d) exhibited a profound increase in photocurrent under the optimum conditions for the electrolyte (Fig. S2). The result of a significantly higher photocurrent density was due to external circuit circumstances, where more photoinduced electrons were transported from the active material of the CdS NPs-Au QDs-2 to the counter electrode [54]. Nevertheless, as the amount of Au QDs is further increased (curve e), the photocurrent response shows a reduction in the current density, indicating the full and excess absorption of Au QDs toward the CdS NPs.
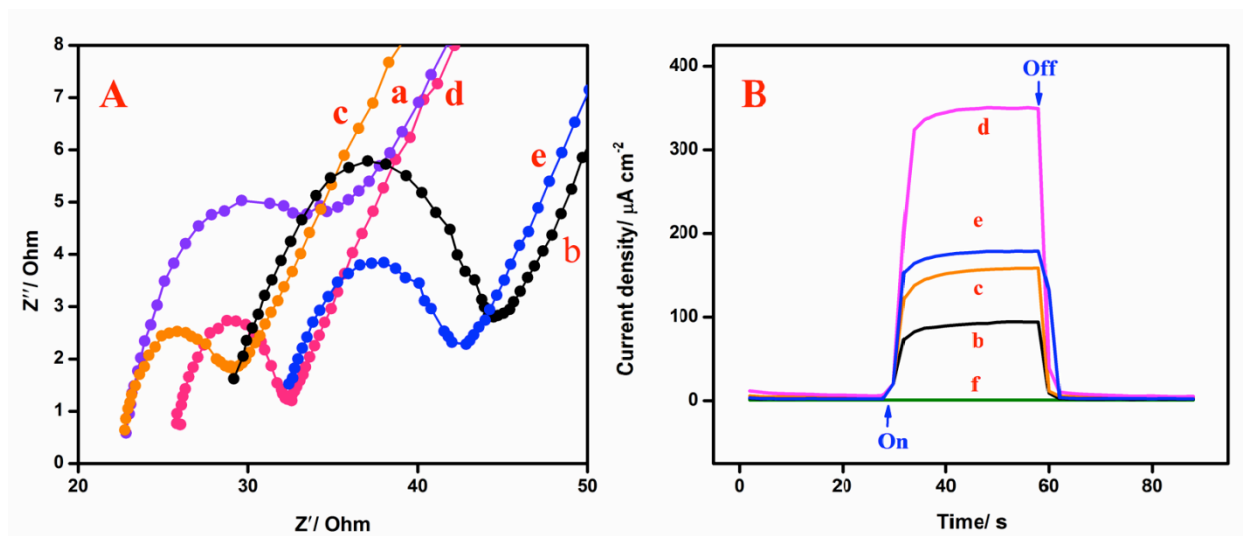
Fig. 6- (A) EIS Nyquist plots of different prepared electrodes in 0.1 M KCl solution containing 5 mM $K_4[Fe(CN)_6]$/ $K_3[Fe(CN)_6]$ and (B) photocurrent responses of as-prepared electrodes in 0.1 M KCl and 0.5 M TEA as electron donor for (a) bare ITO, (b) CdS NPs, (c) CdS NPs-Au QDs-1, (d) CdS NPs-Au QDs-2, (e) CdS NPs-Au QDs-3, and (f) Au QDs.

3.5. Analytical Performance of PEC Sensor

After the CdS NPs were decorated with the Au QDs, the sensing performance of the PEC sensor was investigated and is presented in Fig. 7. Under optimum conditions (see supplementary information, Fig. S3), the CdS NPs-Au QDs-2 photoelectrode was established as a PEC sensor for various concentrations of Cu^{2+}. The time-dependent photocurrent density (I-t) measurements with a linear range concentration of 0.5 to 120 nM Cu^{2+} are presented in Fig. 7A. The photocurrent density was found to decrease with an increasing Cu^{2+} concentration on the photoactive site, and the decrease in photocurrent was mainly attributed to the generation of Cu_xS (X = 1, 2) on the CdS surface which provides a lower energy level and thus led to the recombination electron-hole pair [5]. The detail mechanism of Cu^{2+} ions detection will be further discussed in Section 3.6. Moreover, a good linear relationship of 0.9931 was achieved for ΔI

26

against the Cu^{2+} concentration plot, as shown in Fig. 7B. A limit of detection (LoD) of 6.73 was attained at a signal-to-noise ratio of S/N = 3, which was lower than those of the other modified electrodes of CdS NPs, CdS NPs-Au QDs-1, and CdS NPs-Au QDs-3 (see supplementary information, Table S1). Therefore, the CdS NPs-Au QDs-2 electrode was selected as the optimum photoelectrode for PEC detection because it had the lowest LoD, compared to the other reported electrodes, as listed in Table S2 (see supplementary information). Our CdS NPs-Au QDs-2 electrode showed a good linear relationship, good sensitivity toward Cu^{2+}, and tremendous PEC performance under on-off visible light illumination.

In order to investigate the specificity of this new PEC sensor, various metal ions such as Zn^{2+}, Mn^{2+}, Na^+, Ba^{2+}, Mg^{2+}, K^+, Ni^{2+}, Co^{2+}, Fe^{2+}, Cr^{2+}, Cd^{2+} and Pb^{2+} were selected for interference tests. The metal ion selectivity was determined by measuring the change in the photocurrent response (ΔI) of the CdS-AuNPs-2 toward 120 nM solutions of various metal ions. As shown in Fig. 7C, the ΔI values of Cu^{2+} were very pronounced and caused significant changes in the photocurrent density. However, the photocurrent responses to other interfering ions were very close to that of the blank test. Therefore, it can be deduced from the results of this result that the proposed PEC sensor has good selectivity for Cu^{2+} ion detection. To further determine the selectivity of the modified PEC sensor, the photocurrent responses upon the addition of different interference ions were demonstrated. As displayed in Fig. 7D, a 1.5 nM spike for Cu^{2+} resulted in a rapid and profound photocurrent decrease, whereas a subsequent spike of interference ions at more than 67-fold that of the Cu^{2+} concentration did not cause any measurable response. After that, another 5.0 nM Cu^{2+} was spiked, and an apparent photocurrent decrease was again revealed. This can be explained by the displacement of Cd^{2+} by the aid of the SPR Au QDs, which show a strong absorption in the visible region and thus the formation of MS (for M = Zn, Mn, Na, Ba,

Mg, K, Ni, Co, Fe, Cr, Pb) on the CdS-Au QDs surface. The CdS-AuNPs-2 electrode was proven to be much more sensitive to Cu^{2+} than to other interference ions because Cu_xS has a low K_{sp} value (lower than those of ZnS, MnS, Na_2S, and others) [5]. Therefore, the CdS NPs-Au QDs-2 exhibited excellent anti-interference and possessed a very favorable selectivity toward Cu^{2+} detection.
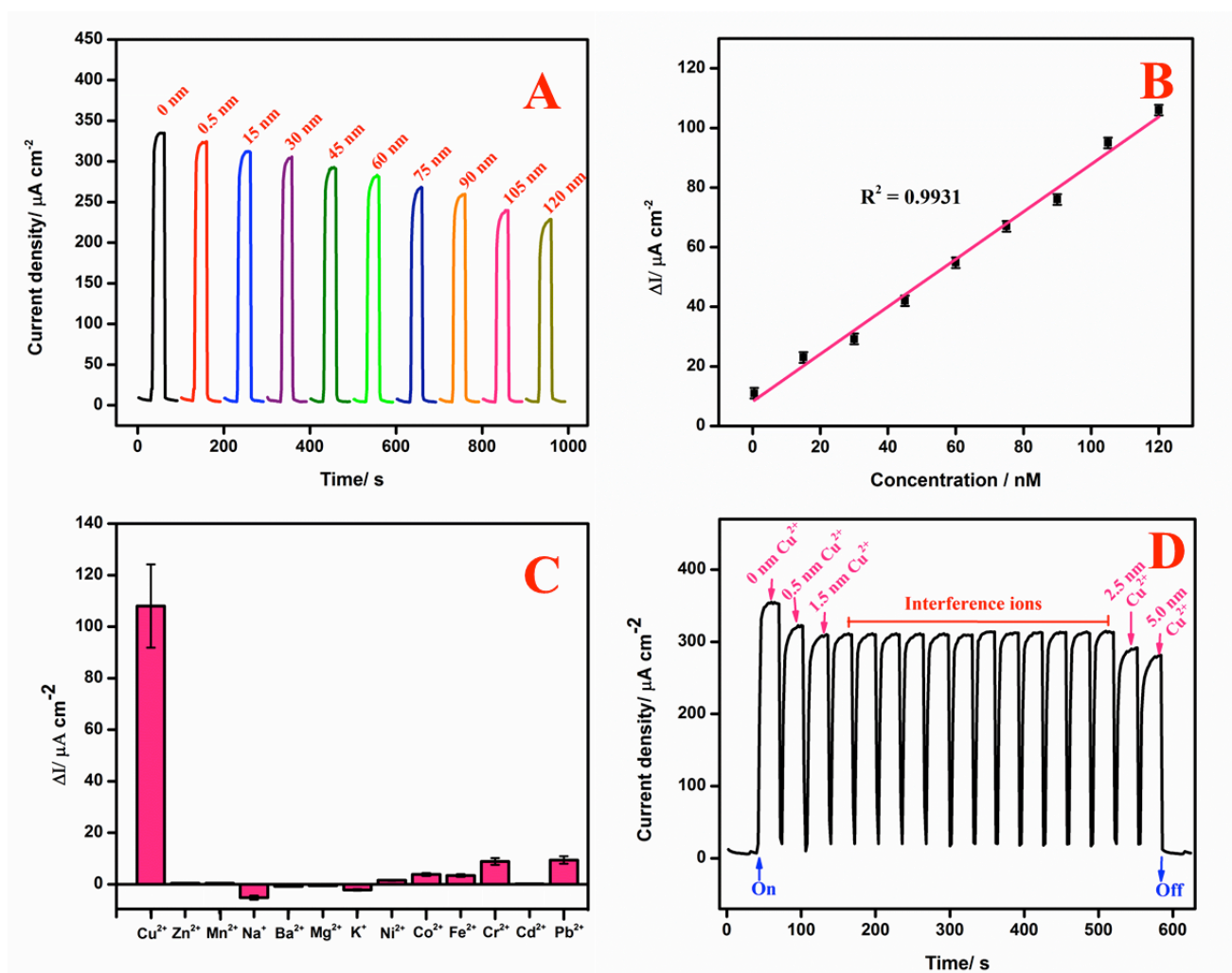

Fig. 7- (A) Photocurrent response of CdS NPs-Au QDs-2 upon detection of various concentrations of target Cu^{2+} and (B) its corresponding calibration curve in linear range concentration of 0.5–120 nM. (C) Selectivity test with interfering substances and (D) anti-

interference test with initial addition of 1.5 nM Cu^{2+} and 0.1 μM of interference ions (Zn^{2+}, Mn^{2+}, Na^+, Ba^{2+}, Mg^{2+}, K^+, Ni^{2+}, Co^{2+}, Fe^{2+}, Cr^{2+}, Cd^{2+} and Pb^{2+}), followed by addition of another 5.0 nM Cu^{2+}.

3.6. Mechanism for Cu^{2+} Detection

In this study, the idea of loading plasmonic Au QDs on CdS NPs was developed in Scheme 1A, and the mechanism for Cu^{2+} ion detection was postulated as illustrated in Scheme 1B. The Au QDs were decorated on the neat spherical surfaces of the CdS NPs through the covalent interaction of Au-S [55], which provided enough stability for the dispersion of narrow size particles and enhanced the PEC efficiency of the as-prepared electrode. It should be noted that the plasmonic effect of the Au QDs demonstrated a remarkable achievement in intensifying the scattering light activity of the CdS semiconductor [56]. As shown in Scheme 1B, under the illumination of light, CdS captures the incident photons to excite the electrons from the valance band to the conduction band, leaving holes at valance band. Simultaneously, the decorated Au QDs capture photons from the incident light of CdS due to the SPR effect. The photoexcited hot electrons in the SPR state are injected ballistically into the conduction band of CdS (due to electromagnetic fields localized between Au and CdS) to trigger the reduction of Cu^{2+} to Cu^+, whereas the photogenerated holes are scavenged by sacrificial agent, TEA, that is present in the electrolyte. In the conduction band of CdS, the formation of Cu_xS (X =1, 2) occurs on the surface of the CdS due to the competitive displacement of Cd^{2+} by Cu^{2+}, hence leading to the formation of Cu_xS-doped CdS. The competitive binding effect and displacement of cation happens due to the lower solubility product of Cu_xS ($K_{sp} = 6 \times 10^{-37}$) than CdS ($K_{sp} = 8 \times 10^{-28}$). The generation of Cu_xS on the CdS surface provides a lower energy level which leads to the existence of electron-hole pair recombination centers, and thus decreases the photocurrent

intensity for electrolyte containing Cu^{2+} ions. Additionally, the continuous transfer of photoexcited hot electrons in the Au to the conduction band of adjacent CdS attributes to the effective energy transfer from the Au QDs to CdS NPs. It also hinders the recombination of electron-hole pairs in the CdS NPs via a stepwise electron-transfer process, therefore increases the output and lifetime of the electrons. Eventually, this phenomenon significantly improves the PEC efficiency of probing Cu^{2+} ions detection using CdS NPs-Au QDs PEC sensor.
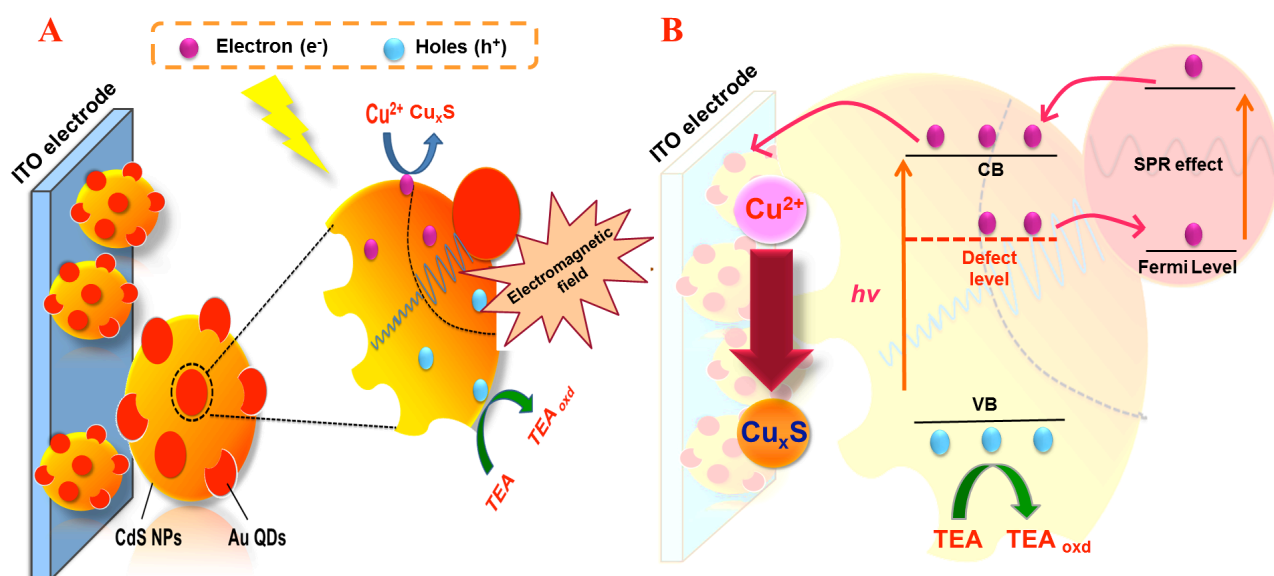
Scheme 1- Interaction of CdS NPs with electromagnetic fields localized at Au QDs when (A) Au is embedded on neat spherical surface of semiconductor. (B) Schematic mechanism for Cu^{2+} ion detection.

3.7. Applicability of Proposed Electrode Sensor

The long-term stability of the proposed PEC sensor was assessed. The photoelectrode sensor was dried and stored in a dark atmosphere at room temperature for different periods. The photocurrent intensity of CdS NPs-Au QDs-2 showed a slight decrease as the storage time was

increased from 1 to 8 weeks. The current response was observed to decrease to 3.07% after 1 week of storage. However, after storage for 4 and 8 weeks the photoelectrode was shown to still retain about 85.1% and 73% of its initial response, respectively. Therefore, the photoelectrode sensor showed no significant photocurrent deterioration after 8 weeks of storage in a dark atmosphere, which indicates that the photoelectrode sensor has good storage stability because of the potent synergic interaction between the CdS NPs and Au QDs.

Additionally, another crucial analysis for practical applications involved a reproducibility test of the modified photoelectrode sensor. The inter-assay precision of five replicates of the proposed PEC sensors was investigated in the absence and presence of 120 nM Cu^{2+}. Under the same condition, the photocurrent response demonstrated similar photocurrents with relative standard deviations (RSD) of 9.6% and 9.3%, respectively. It was proven that the CdS NPs-Au QDs-2 photoelectrode sensor had good fabrication reproducibility.

The feasibility of the proposed sensor was further examined using real sample analysis. The CdS-decorated Au QDs photoelectrode was used to detect Cu^{2+} in tap and lake water samples using the standard addition method. As presented in Table 2, different concentrations of Cu^{2+} were added to the lake and tap water samples, and the obtained recoveries of the PEC sensor were in the range of 97.6–120.8%. Accordingly, the proposed PEC sensor had a good performance in real sample detection, showing promise for potential applications in environmental monitoring and analysis.

Table 2- Results of Cu^{2+} detection in lake and tap water using as-prepared PEC sensor.

Sample	Cu^{2+} added (nM)	Cu^{2+} found (nM)	RSD% (n=3)	Recovery (%)
Lake water	30	29.3	6.3	97.6
	60	72.5	5.5	120.8
	90	89.0	7.5	98.8
	120	122.9	4.6	102.4
Tap water	30	30.0	3.8	100.1
	60	61.9	3.9	103.2
	90	89.7	7.1	99.7
	120	119.1	14.8	99.3

4. Conclusions

Conclusively, a novel and simple method was established based on CdS NPs decorated on Au QDs for the PEC detection of Cu^{2+} with high sensitivity and selectivity. This PEC sensor displayed excellent analytical performance. It not only showed high sensitivity and good selectivity, but also revealed a robust stability, better anti-interference, and good fabrication reproducibility. Furthermore, the remarkable photocurrent response of the hybrid semiconductor CdS and noble metal Au was due to the plasmonic effect of Au in enhancing the scattering light activity of the CdS semiconductor. The PEC method showed a low detection limit of 6.73 nM for Cu^{2+} sensing in a good linear range concentration of 0.5–120 nM. In addition, the as-prepared PEC sensor was satisfactorily used to detect the content of Cu^{2+} in tap and lake water samples. This strategy was found to be simple, fast, cost-effective, and ultrasensitive, which paves the way for a new channel in developing high-performance PEC based on nanostructure materials.

Supporting Information

The EDX spectrum of CdS NPs decorated Au QDs and TEM image of flawless structure of CdS NPs are shown in Fig. S1. Fig. S2 illustrated the photocurrent response of CdS NPs-Au QDs-2 in air-saturated and nitrogen-saturated solution; and in the presence and absence of TEA as sacrificial electron donor. The effect of hydrothermal temperature, TEA concentration as sacrificial electron donor, the applied voltage and the photocurrent density-time graph for different applied voltage was studied and the result was demonstrated in Fig. S3. The LoD results for the as-prepared elctrode (S/N=3) was tabulated in Table S1. Table S2 shows the comparison of different methods for Cu^{2+} detection.

References

1.   McMichael, A. J. The Urban Environment and Health in a World of Increasing Globalization: Issues for Developing Countries. *Bulletin of the World Health Organization* 2000, *78*, 1117-1126.

2.   Li, J.; Zhao, T.; Chen, T.; Liu, Y.; Ong, C. N.; Xie, J. Engineering Noble Metal Nanomaterials for Environmental Applications. *Nanoscale* 2015, *7*, 7502-7519.

3.   Xin, Y.; Li, Z.; Zhang, Z. Photoelectrochemical Aptasensor for the Sensitive and Selective Detection of Kanamycin Based on Au Nanoparticle Functionalized Self-Doped TiO_2 Nanotube Arrays. *Chem. Commun* 2015, *51*, 15498-15501.

4.   Huang, F.; Pu, F.; Lu, X.; Zhang, H.; Xia, Y.; Huang, W.; Li, Z. Photoelectrochemical Sensing of Cu^{2+} Ions with SnO_2/CdS Heterostructural Films. *Sens. Actuators. B* 2013, *183*, 601-607.

5.   Shen, Q.; Zhao, X.; Zhou, S.; Hou, W.; Zhu, J. J. ZnO/CdS Hierarchical Nanospheres for Photoelectrochemical Sensing of Cu^{2+}. *J. Phys. Chem. C* 2011, *115*, 17958-17964.

6.   Tang, J.; Li, J.; Zhang, Y.; Kong, B.; Wang, Y.; Quan, Y.; Cheng, H.; Al-Enizi, A. M.; Gong, X.; Zheng, G. Mesoporous Fe_2O_3–CdS Heterostructures for Real-Time Photoelectrochemical Dynamic Probing of Cu^{2+}. *Anal. chem* 2015, *87*, 6703-6708.

7.   Ibrahim, I.; Lim, H.; Huang, N.; Pandikumar, A. Cadmium Sulphide-Reduced Graphene Oxide-Modified Photoelectrode-Based Photoelectrochemical Sensing Platform for Copper (II) Ions. *PloS one* 2016, *11*, e0154557.

8.   Marcus, P., *Corrosion Mechanisms in Theory and Practice*; CRC Press, Boca Raton, Florida, 2011.

9.   Li, L.; Salvador, P. A.; Rohrer, G. S. Photocatalysts with Internal Electric Fields. *Nanoscale* 2014, *6*, 24-42.

10.   Auffan, M.; Rose, J.; Bottero, J. Y.; Lowry, G. V.; Jolivet, J. P.; Wiesner, M. R. Towards a Definition of Inorganic Nanoparticles from an Environmental, Health and Safety Perspective. *Nat. nanotech* 2009, *4*, 634-641.

11. Ghosh Chaudhuri, R.; Paria, S. Core/Shell Nanoparticles: Classes, Properties, Synthesis Mechanisms, Characterization, and Applications. *Chem rev* 2011, *112*, 2373-2433.

12. Wang, H.; Sun, Z.; Lu, Q.; Zeng, F.; Su, D. One-Pot Synthesis of (Au Nanorod)–(Metal Sulfide) Core–Shell Nanostructures with Enhanced Gas-Sensing Property. *Small* 2012, *8*, 1167-1172.

13. Wu, X.; He, X.; Wang, K.; Xie, C.; Zhou, B.; Qing, Z. Ultrasmall near-Infrared Gold Nanoclusters for Tumor Fluorescence Imaging in Vivo. *Nanoscale* 2010, *2*, 2244-2249.

14. Lee, J. C.; Sung, Y. M.; Kim, T. G.; Choi, H. J. TiO_2-CdSe Nanowire Arrays Showing Visible-Range Light Absorption. *Appl. Phys. Lett* 2007, *91*, 3104.

15. Liu, C.; Tang, H.; Li, J.; Li, W.; Yang, Y.; Li, Y.; Chen, Q. Enhancing Photoelectrochemical Activity of CdS Quantum Dots Sensitized Wo_3 Photoelectrodes by Mn Doping. *RSC Adv* 2015, *5*, 35506-35512.

16. Ahire, R.; Deshpande, N.; Gudage, Y.; Sagade, A.; Chavhan, S.; Phase, D.; Sharma, R. A Comparative Study of the Physical Properties of CdS, Bi_2S_3 and Composite CdS–Bi_2S_3 Thin Films for Photosensor Application. *Sens. Actuators. A* 2007, *140*, 207-214.

17. Travas S. J.; Peng, H.; Cooney, R.; Bowmaker, G.; Cannell, M.; Soeller, C. Amplification of a Conducting Polymer-Based DNA Sensor Signal by CdS Nanoparticles. *Curr. Appl. Phys* 2006, *6*, 562-566.

18. Smyntyna, V.; Gerasutenko, V.; Kashulis, S.; Mattogno, G.; Reghini, S. The Causes of Thickness Dependence of CdSe and CdS Gas-Sensor Sensitivity to Oxygen. *Sens. Actuators. B* 1994, *19*, 464-465.

19.   Dobson, K. D.; Visoly F. I.; Hodes, G.; Cahen, D. Stability of CdTe/CdS Thin-Film Solar Cells. *Solar Energy Mater. Solar Cells* 2000, *62*, 295-325.

20.   Zhao, W. W.; Wang, J.; Xu, J. J.; Chen, H. Y. Energy Transfer between CdS Quantum Dots and Au Nanoparticles in Photoelectrochemical Detection. *Chem. Commun* 2011, *47*, 10990-10992.

21.   Zayats, M.; Kharitonov, A. B.; Pogorelova, S. P.; Lioubashevski, O.; Katz, E.; Willner, I. Probing Photoelectrochemical Processes in Au-CdS Nanoparticle Arrays by Surface Plasmon Resonance: Application for the Detection of Acetylcholine Esterase Inhibitors. *J. Am. Chem. Soc* 2003, *125*, 16006-16014.

22.   Yin, X. L.; Liu, J.; Jiang, W. J.; Zhang, X.; Hu, J.-S.; Wan, L. J. Urchin-Like Au@CdS/WO$_3$ Micro/Nano Heterostructure as a Visible-Light Driven Photocatalyst for Efficient Hydrogen Generation. *Chem. Commun* 2015, *51*, 13842-13845.

23.   Kiyonaga, T.; Akita, T.; Tada, H. Au Nanoparticle Electrocatalysis in a Photoelectrochemical Solar Cell Using CdS Quantum Dot-Sensitized TiO$_2$ Photoelectrodes. *Chem, Commun* 2009, 2011-2013.

24.   Xing, X.; Liu, R.; Yu, X.; Zhang, G.; Cao, H.; Yao, J.; Ren, B.; Jiang, Z.; Zhao, H. Self-Assembly of CdS Quantum Dots with Polyoxometalate Encapsulated Gold Nanoparticles: Enhanced Photocatalytic Activities. *J. Mater. Chem. A* 2013, *1*, 1488-1494.

25.   Pu, Y.; Zhang, J. Mechanisms Behind Plasmonic Enhancement of Photocurrent in Metal Oxides. *Austin J. Nanomed. Nanotechnol* 2014, *2*, 1030.

26.   Zhuang, J.; Tang, D.; Lai, W.; Xu, M.; Tang, D. Target-Induced Nano-Enzyme Reactor Mediated Hole-Trapping for High-Throughput Immunoassay Based on a Split-Type Photoelectrochemical Detection Strategy. *Anal. chem* 2015, *87*, 9473-9480.

27.   Zhu, Y. C.; Zhang, N.; Ruan, Y. F.; Zhao, W. W.; Xu, J. J.; Chen, H. Y. Alkaline Phosphatase Tagged Antibodies on Gold Nanoparticles/Tio2 Nanotubes Electrode: A Plasmonic Strategy for Label-Free and Amplified Photoelectrochemical Immunoassay. *Anal. chem* 2016, *88*, 5626–5630.

28.   Zhao, M.; Fan, G. C.; Chen, J. J.; Shi, J. J.; Zhu, J. J. Highly Sensitive and Selective Photoelectrochemical Biosensor for Hg^{2+} Detection Based on Dual Signal Amplification by Exciton Energy Transfer Coupled with Sensitization Effect. *Anal. chem* 2015, *87*, 12340-12347.

29.   Guo, Y.; Zhang, Y.; Shao, H.; Wang, Z.; Wang, X.; Jiang, X. Label-Free Colorimetric Detection of Cadmium Ions in Rice Samples Using Gold Nanoparticles. *Anal. chem* 2014, *86*, 8530-8534.

30.   Frens, G. Controlled Nucleation for the Regulation of the Particle Size in Monodisperse Gold Suspensions. *Nature* 1973, *241*, 20-22.

31.   Yu, K.; Polavarapu, L.; Xu, Q. H. Excitation Wavelength and Fluence Dependent Femtosecond Transient Absorption Studies on Electron Dynamics of Gold Nanorods. *J. Phys. Chem. A* 2011, *115*, 3820-3826.

32.   Shin, H. J.; Hwang, I. W.; Hwang, Y. N.; Kim, D.; Han, S. H.; Lee, J. S.; Cho, G. Comparative Investigation of Energy Relaxation Dynamics of Gold Nanoparticles and Gold-Polypyrrole Encapsulated Nanoparticles. *J. Phys. Chem. B* 2003, *107*, 4699-4704.

33.   Link, S.; El-Sayed, M. A.; Schaaff, T. G.; Whetten, R. L. Transition from Nanoparticle to Molecular Behavior: A Femtosecond Transient Absorption Study of a Size-Selected 28 Atom Gold Cluster. *Chem. phys. lett* 2002, *356*, 240-246.

34.   Guo, Y.; Wang, J.; Tao, Z.; Dong, F.; Wang, K.; Ma, X.; Yang, P.; Hu, P.; Xu, Y.; Yang, L. Facile Synthesis of Mesoporous CdS Nanospheres and Their Application in Photocatalytic Degradation and Adsorption of Organic Dyes. *CrystEngComm* 2012, *14*, 1185-1188.

35.   Park, J.; Park, S.; Selvaraj, R.; Kim, Y. Microwave-Assisted Synthesis of Au/CdS Nanorods for a Visible-Light Responsive Photocatalyst. *RSC Adv* 2015, *5*, 52737-52742.

36.   Huang, X.; El-Sayed, M. A. Gold Nanoparticles: Optical Properties and Implementations in Cancer Diagnosis and Photothermal Therapy. *J. Adv. Res* 2010, *1*, 13-28.

37.   Wang, X.; Ying, Y.; Lei, J.; Hu, P.; Peng, X. Starfish-Like Au–CdS Hybrids for the Highly Efficient Photocatalytic Degradation of Organic Dyes. *RSC Adv* 2014, *4*, 42441-42444.

38.   Szeremeta, J.; Nyk, M.; Wawrzynczyk, D.; Samoc, M. Wavelength Dependence of Nonlinear Optical Properties of Colloidal Cds Quantum Dots. *Nanoscale* 2013, *5*, 2388-2393.

39.   Haiss, W.; Thanh, N. T.; Aveyard, J.; Fernig, D. G. Determination of Size and Concentration of Gold Nanoparticles from UV-Vis Spectra. *Anal. chem* 2007, *79*, 4215-4221.

40.   López L. Á. I.; Soriano, M. L.; Valcárcel, M. Analysis of Citrate-Capped Gold and Silver Nanoparticles by Thiol Ligand Exchange Capillary Electrophoresis. *Microchim. Acta* 2014, *181*, 1789-1796.

41.   Naveenraj, S.; Anandan, S.; Kathiravan, A.; Renganathan, R.; Ashokkumar, M. The Interaction of Sonochemically Synthesized Gold Nanoparticles with Serum Albumins. *J. pharm. biomed. anal* 2010, *53*, 804-810.

42.   Pandikumar, A.; Ramaraj, R. Photocatalytic Reduction of Hexavalent Chromium at Gold Nanoparticles Modified Titania Nanotubes. *Mater. Chem. Phys* 2013, *141*, 629-635.

43.   Lakowicz, J. R. Radiative Decay Engineering: Biophysical and Biomedical Applications. *Anal. biochem* 2001, *298*, 1-24.

44.   Paul, R.; Kumbhakar, P.; Mitra, A. Visible Photoluminescence of MWCNT/CdS Nanohybrid Structure Synthesized by a Simple Chemical Process. *Mater. Sci. Eng. B* 2010, *167*, 97-101.

45.   Dana, J.; Debnath, T.; Maity, P.; Ghosh, H. N. Enhanced Charge Separation in an Epitaxial Metal–Semiconductor Nanohybrid Material Anchored with an Organic Molecule. *J. Phys. Chem. C* 2015, *119*, 22181-22189.

46.   Lu, Y.; Jia, J.; Yi, G. Selective Growth and Photoelectrochemical Properties of Bi_2S_3 Thin Films on Functionalized Self-Assembled Monolayers. *CrystEngComm* 2012, *14*, 3433-3440.

47.   Liu, B.; Li, X. B.; Gao, Y. J.; Li, Z. J.; Meng, Q. Y.; Tung, C. H.; Wu, L. Z. A Solution-Processed, Mercaptoacetic Acid-Engineered CdSe Quantum Dot Photocathode for Efficient Hydrogen Production under Visible Light Irradiation. *Energy Environ. Sci* 2015, *8*, 1443-1449.

48.   Zhang, S.; Xu, G.; Gong, L.; Dai, H.; Li, Y.; Hong, Z.; Lin, Y. TiO_2-B Nanorod Based Competitive-Like Non-Enzymatic Photoelectrochemical Sensing Platform for Noninvasive Glucose Detection. *J. Mater.Chem. B* 2015, *3*, 7554-7559.

49.   Hu, Z.; Xu, M.; Shen, Z.; Yu, J. A Nanostructured Chromium (III) Oxide/Tungsten (VI) Oxide p-n Junction Photoanode toward Enhanced Faradaic Efficiency for Water Oxidation. *J. Mater. Chem. A* 2015, *3*, 14046-14053.

50.   Jiang, N.; Xiu, Z.; Xie, Z.; Li, H.; Zhao, G.; Wang, W.; Wu, Y.; Hao, X. Reduced Graphene Oxide–CdS Nanocomposites with Enhanced Visible-Light Photoactivity Synthesized Using Ionic-Liquid Precursors. *New J. Chem* 2014, *38*, 4312-4320.

51.   Shen, Q.; Jiang, J.; Liu, S.; Han, L.; Fan, X.; Fan, M.; Fan, Q.; Wang, L.; Huang, W. Facile Synthesis of Au–SnO_2 Hybrid Nanospheres with Enhanced Photoelectrochemical Biosensing Performance. *Nanoscale* 2014, *6*, 6315-6321.

52.   Khaselev, O.; Turner, J. A. A Monolithic Photovoltaic-Photoelectrochemical Device for Hydrogen Production Via Water Splitting. *Science* 1998, *280*, 425-427.

53.   Zhao, W. W.; Wang, J.; Xu, J. J.; Chen, H. Y. Energy Transfer between CdS Quantum Dots and Au Nanoparticles in Photoelectrochemical Detection. *Chem.Commun* 2011, *47*, 10990-10992.

54.   Zhao, M.; Li, H.; Shen, X.; Ji, Z.; Xu, K. Facile Electrochemical Synthesis of CeO_2@Ag@CdS Nanotube Arrays with Enhanced Photoelectrochemical Water Splitting Performance. *Dalton Trans.* 2015, *44*, 19935-19941.

55. Noda, Y.; Noro, S. i.; Akutagawa, T.; Nakamura, T. Gold Nanoparticle Assemblies Stabilized by Bis(Phthalocyaninato) Lanthanide (III) Complexes through Van Der Waals Interactions. *Scientific rep.* 2014, *4*, 3758.

56. Yu, G.; Wang, X.; Cao, J.; Wu, S.; Yan, W.; Liu, G. Plasmonic Au Nanoparticles Embedding Enhances the Activity and Stability of CdS for Photocatalytic Hydrogen Evolution. *Chem. Commun* 2015, *52*, 2394-2397.

TOC graphic